Rigorous formalism of anharmonic atomistic Green's function for three-dimensional interfaces

Jinghang Dai and Zhiting Tian

Phys. Rev. B **101**, 041301 — Published 13 January 2020

DOI: 10.1103/PhysRevB.101.041301

A rigorous formalism of anharmonic atomistic Green's function for 3-D interfaces

Jinghang Dai and Zhiting Tian*

Sibley School of Mechanical and Aerospace Engineering, Cornell University, NY 14853, USA
** Address all correspondence to Zhiting Tian's E-mail: zhiting@cornell.edu*

Abstract: The traditional atomistic Green's function (AGF) was formulated in the harmonic regime, preventing it from capturing the role of anharmonicity in interfacial thermal transport. Incorporating anharmonicity into AGF has long been desired but remains challenging. In this work, we developed an anharmonic AGF model to incorporate anharmonicity at interfaces in 3-D structures rigorously. Without any fitting parameters, we can obtain the thermal interface conductance using first-principle force constants as the only inputs. This work represents a significant step forward for AGF.

Keywords: atomistic Green's function, anharmonicity, interfacial thermal transport

Introduction

Heat dissipation in microelectronics is a critical issue that limits their performance and reliability [1]. Massive resistance at solid-solid interfaces often presents the major bottleneck for heat removal [2]. Therefore, understanding interfacial thermal transport and engineering interfaces to reach ultrahigh thermal conductance are in great demand. Atomistic Green's function (AGF) has been a powerful tool to study nanoscale thermal transport [3,4], especially across interfaces. However, the traditional AGF [3,5–12] was formulated within the harmonic regime. The lack of anharmonicity has been a major limitation for AGF to treat interfacial thermal transport in the practical temperature ranges [13,14]. Including anharmonicity in AGF is in principle possible, but very challenging. Since Mingo included anharmonicity for a 1-D atomic junction in 2006 [15], there have been few attempts to include anharmonicity for 3-D structures using different levels of approximation, such as obtaining the anharmonic potential energy or inelastic phonon scattering rates by fitting the experimental data [16–18]. Those studies showed the importance of anharmonicity on interfacial thermal transport and inspired our efforts to include anharmonicity in AGF without any approximation.

In this paper, we developed a rigorous formalism of anharmonic AGF to treat the inelastic phonon scattering processes at 3-D interfaces. We explicitly derived all the equations in the fully quantum mechanical regime. Without any fitting parameters, we incorporated both harmonic and anharmonic first-principles force constants into AGF. To include many-body interactions via Keldysh formalism [19–22], we formulated a new Fourier decomposition method for 3rd order tensors and defined the many-body self-energy for 3-D structures in reciprocal space. This new decomposition method dramatically reduces the otherwise prohibited computational load and allows us to accurately account for the inelastic phonon scattering using first-principles force constants. We then applied the anharmonic AGF to 3-D silicon- (Si) and aluminum- (Al) based interfaces as a demonstration. We obtained a consistent result with earlier studies that anharmonicity enhances interfacial thermal transport on Si/germanium (Ge) interfaces [23]. Moreover, by employing our method, we demonstrated the increase of heat current at different frequencies and quantitatively explained the intrinsic mechanism of this enhancement using the overlap of phonon density of states (DoS). The 3-D anharmonic AGF method we present here paves the way for AGF studies of interfacial thermal transport when anharmonicity is not negligible.

Method derivation

1-D harmonic AGF—In a traditional AGF model, the system is composed of two semi-infinite leads and one central region. The physical interface is in the central region. Retarded Green's function, $\boldsymbol{G}^r$, describes the dynamics of phonons in the central region, taking the effect of the leads into account through self-energies:

$$\boldsymbol{G}^r = [\omega^2 \boldsymbol{I} - \boldsymbol{H}_C - \boldsymbol{\Sigma}_L^r - \boldsymbol{\Sigma}_R^r]^{-1} \tag{1}$$

where $\boldsymbol{\Sigma}_{L(R)}^r \equiv \boldsymbol{H}_{CL(CR)} \boldsymbol{g}_{L(R)}^r \boldsymbol{H}_{LC(RC)}$. $\boldsymbol{H}_{CL(CR)}$, $\boldsymbol{H}_{LC(RC)}$ are harmonic force constant matrices connecting the left or right lead to the central region, and $\boldsymbol{g}_{L(R)}^r$ is the uncoupled retarded Green's function for the semi-infinite leads. For detailed information, please refer to Ref [3].

1-D anharmonic AGF—To account for the contribution from three-phonon scattering for 1-D structures, the many-body self-energy, $\boldsymbol{\Sigma}_M^r$, is added into the total self-energy [15]: $\boldsymbol{G}^r = [\omega^2\boldsymbol{I} - \boldsymbol{H}_C - \boldsymbol{\Sigma}_L^r - \boldsymbol{\Sigma}_R^r - \boldsymbol{\Sigma}_M^r]^{-1}$. We can obtain $\boldsymbol{\Sigma}_M^r$ from the coupled non-equilibrium Green's functions, $\boldsymbol{G}^<$ and $\boldsymbol{G}^>$ (lesser and greater Green's functions), and the 3rd order anharmonic tensor of the central region, $\boldsymbol{\mathcal{V}}_{ijk}$ (*i, j, k* are the indices for 3rd order tensor). For non-equilibrium Green's function calculation, the temperature at both leads is different. The temperature information of the leads represented by Bose-Einstein distribution is already included in the uncoupled Green's functions, $\boldsymbol{g}_{L(R)}^<$ and $\boldsymbol{g}_{L(R)}^>$. As a validation of our method, we reproduced Mingo's results for the 1-D chain in Supplementary Materials [24,25].

3-D harmonic AGF—We borrowed the idea of using the $\boldsymbol{P}$ matrix for the Fourier decomposition. This method was applied to investigate the harmonic phonon transmission in carbon nanotube junctions [10]. We extended the $\boldsymbol{P}$ matrix method to 3-D structures by defining $P(\vec{R}_a, \vec{Q}_\alpha) = \frac{1}{N} I_H e^{i\vec{R}_a \cdot \vec{Q}_\alpha}$, where $\vec{R}_a$ is the unit cell position vector, $\vec{Q}_\alpha$ is the transverse wave vector, and N is the number of unit cells along the transverse direction. Via the equation $\widetilde{\boldsymbol{H}} = \boldsymbol{P}^{-1}\boldsymbol{H}\boldsymbol{P}$, we have:

$$\tilde{H}(\vec{Q}_\alpha) = \sum_{a=1}^{N^2}\sum_{b=1}^{N^2} H(\vec{R}_a, \vec{R}_b) e^{-i\vec{Q}_\alpha \cdot (\vec{R}_a - \vec{R}_b)} \tag{2}$$

Through this method, we only need one wave vector $\vec{Q}_\alpha$ to represent all the Green's functions and self-energies in reciprocal space. One can find the derivation in Supplementary Materials [24,26,27].

3-D anharmonic AGF—Instead of approximating the inelastic phonon scattering, we built our method upon the 1-D anharmonic AGF method. Well-established tensor decomposition methods [28] such as higher-order singular value decomposition (HOSVD) or canonical/parallel factor (CP) decomposition all fall short of reducing the dimension of the 3rd order tensor, $\boldsymbol{\mathcal{V}}_{ijk}$, into the Fourier-component patterns [29]. Therefore, we developed a new 3rd order tensor Fourier decomposition using the $\boldsymbol{P}$ matrix from scratch. For any anharmonic tensor $\boldsymbol{\mathcal{V}}$ or $\mathcal{V}(\vec{R}_a, \vec{R}_b, \vec{R}_c)$ of 3-D structures, the 3rd order tensor Fourier decomposition will be:

$$\tilde{\boldsymbol{\mathcal{V}}}_{uvw} = \sum_{ijk} \boldsymbol{\mathcal{V}}_{ijk} \boldsymbol{P}_{ui}^{-1} \boldsymbol{P}_{vj}^{-1} \boldsymbol{P}_{wk} \text{ or } \tilde{\boldsymbol{\mathcal{V}}}_{pqr} = \sum_{lmn} \boldsymbol{\mathcal{V}}_{lmn} \boldsymbol{P}_{pl}^{-1} \boldsymbol{P}_{qm} \boldsymbol{P}_{rn} \tag{3}$$

By doing so, we only need two wave vectors, $\vec{Q}_\psi$ and $\vec{Q}_\theta$, to represent such 3rd order tensor $\mathcal{V}(\vec{R}_a, \vec{R}_b, \vec{R}_c)$ in real space as $\tilde{\mathcal{V}}(\vec{Q}_\psi, \vec{Q}_\theta)$ in reciprocal space. For detailed derivation, please refer to Supplementary Materials [24,30].

Accordingly, we defined the lesser(greater) many-body self-energy in reciprocal space as:

$$\tilde{\Sigma}_{M,u,r}^{<(>)}(\omega, \vec{Q}) = i\hbar \int_{-\infty}^{\infty} \sum_{\vec{Q}'} \sum_{vwpq} \left[\tilde{\mathcal{V}}_{uvw}(\vec{Q}, \vec{Q}') \tilde{G}_{wp}^{<(>)}(\omega - \omega', \vec{Q}') \mathcal{V}_{pqr}(\vec{Q}, \vec{Q}') \tilde{G}_{qv}^{<(>)}(\omega', \vec{Q}') \right] d\omega' \tag{4}$$

This Fourier decomposition method for 3rd order tensors allows us to rigorously incorporate the anharmonic interactions in the central region into AGF for 3-D structures without any

approximation. Concise analytic expressions for computing many-body Green's function and self-energy matrices in reciprocal space are given as:

$$\tilde{G}^{<(>)}(\omega,\vec{Q}) = \tilde{G}^{r}(\omega,\vec{Q})\tilde{\Sigma}^{<(>)}(\omega,\vec{Q})\left(\tilde{G}^{r}(\omega,\vec{Q})\right)^{\dagger} \quad (5)$$

$$\tilde{G}^{r}(\omega,\vec{Q}) = \left[\omega^2 I - \tilde{H}_C(\vec{Q}) - \tilde{\Sigma}_L^{r}(\omega,\vec{Q}) - \tilde{\Sigma}_R^{r}(\omega,\vec{Q}) - \tilde{\Sigma}_M^{r}(\omega,\vec{Q})\right]^{-1} \quad (6)$$

$$Im\left[\tilde{\Sigma}_M^{r}(\omega,\vec{Q})\right] = \frac{\tilde{\Sigma}_M^{>}(\omega,\vec{Q}) - \tilde{\Sigma}_M^{<}(\omega,\vec{Q})}{2i},\ Re\left[\tilde{\Sigma}_M^{r}(\omega,\vec{Q})\right] = \int_{-\infty}^{\infty} p.v.\left(\frac{1}{\omega-\omega'}\right) \times \frac{-1}{\pi} Im\left[\tilde{\Sigma}_M^{r}(\omega',\vec{Q})\right] d\omega' \quad (7)$$

where the symbol "†" means conjugate transpose and "*p.v.*" means Cauchy principal value. Together with Eq.(4), a self-consistent calculation [15,20] is required to obtain $\tilde{G}^{<(>)}$, from which we can calculate the heat current density on the left or right side of the interface:

$$J_{L(R)}(\omega) = +(-)\sum_{\vec{Q}} \mathrm{Tr}\left[\tilde{\Sigma}_{L(R)}^{>}(\omega,\vec{Q})\tilde{G}^{<}(\omega,\vec{Q}) - \tilde{\Sigma}_{L(R)}^{<}(\omega,\vec{Q})\tilde{G}^{>}(\omega,\vec{Q})\right]\frac{\hbar\omega}{2\pi} \quad (8)$$

The integral of current density over frequency yields the total heat current, which is required to determine the two-probe thermal conductance:

$$\sigma = \lim_{T_L \to T_R} \frac{1}{T_L - T_R}\frac{1}{N^2 A_s}\int_0^{\infty} d\omega \sum_{\vec{Q}} \mathrm{Tr}\left[\tilde{\Sigma}_{L(R)}^{>}(\omega,\vec{Q})\tilde{G}^{<}(\omega,\vec{Q}) - \tilde{\Sigma}_{L(R)}^{<}(\omega,\vec{Q})\tilde{G}^{>}(\omega,\vec{Q})\right]\frac{\hbar\omega}{2\pi} \quad (9)$$

Note that we set the temperature difference to be a small value (0.01K) in this work. With a finite temperature bias, one can even study the thermal rectification effects in the quantum limit.

Results and Discussions

We first employed our anharmonic AGF method on the Si/Ge interface in the [100] direction. The system is schematically depicted in the inset of Fig. 1(b). We used the lattice constant and force constants of Si on both sides, the mass of Si on one side and the mass of Ge on the other side. We calculated the 2nd order force constants via QUANTUM ESPRESSO [31,32] along with Phonopy [33], and the 3rd order force constants from thirdorder.py [34]. We computed the two-probe thermal conductance of the central region as a function of temperature in Fig. 1(a). Both harmonic and anharmonic conductance first rises with temperature, then stays constant because of fully excited modes following the Bose-Einstein distribution. As shown in Fig. 1(b), anharmonicity can enhance the thermal conductance at room temperature, which is consistent with the very recent observation from non-equilibrium molecular dynamics simulations [23]. Due to the anharmonicity, the bulk-like part of the central region also contributes to the total thermal resistance. As a result, the thermal resistance of the physical interface will be even smaller than the value in Fig. 1(a). The central region was set as one unit-cell length in this work just as a demonstration of our method. The bulk-like contribution will not influence the 3-D anharmonic AGF method itself or our main conclusions. One can set the central region long enough to mimic the real device. The application to real devices and extracting thermal resistance of the physical interface will be discussed in our follow-up work.

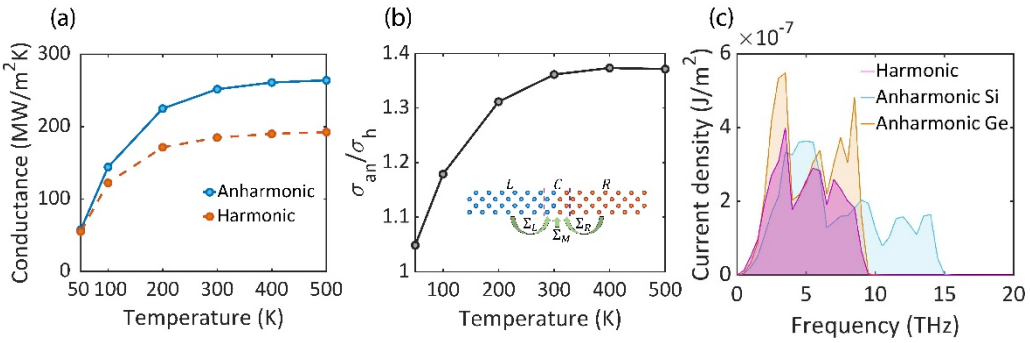

FIG. 1 (a) Conductance of Si/Ge interface, in the absence and presence of anharmonicity in the central region, as a function of temperature. (b) Conductance ratio versus temperature. Inset is the illustration of the system, where the semi-infinite left side (L) is Si meanwhile the right (R) is Ge. The central region (C) contains the interface. (c) Heat current frequency distribution of the harmonic case, in which heat flow is the same on both sides, and the anharmonic heat flow on Si and Ge side.

Besides the thermal conductance, our 3-D anharmonic AGF gives the frequency-resolved anharmonic heat current information without any fitting parameters. In Fig. 1(c), the harmonic heat current remains the same before and after the interface because phonons can only propagate through the interface via elastic processes. After adding anharmonicity to the central region, the current distribution on both sides is no longer the same. On the Si side, the phonon channels with frequencies higher than the cutoff frequency of Ge are opened, and the allowed phonon channels cover the entire frequency range of pure Si. On the Ge side, even though the frequency range remains unchanged, the peaks become more prominent because of the newly opened channels via anharmonicity. Here the anharmonic interface acts as a source of phonon-phonon coupling, which facilitates the energy communication among different phonon modes and assists those blocked phonons in the harmonic limit to propagate through the interface via inelastic scattering.

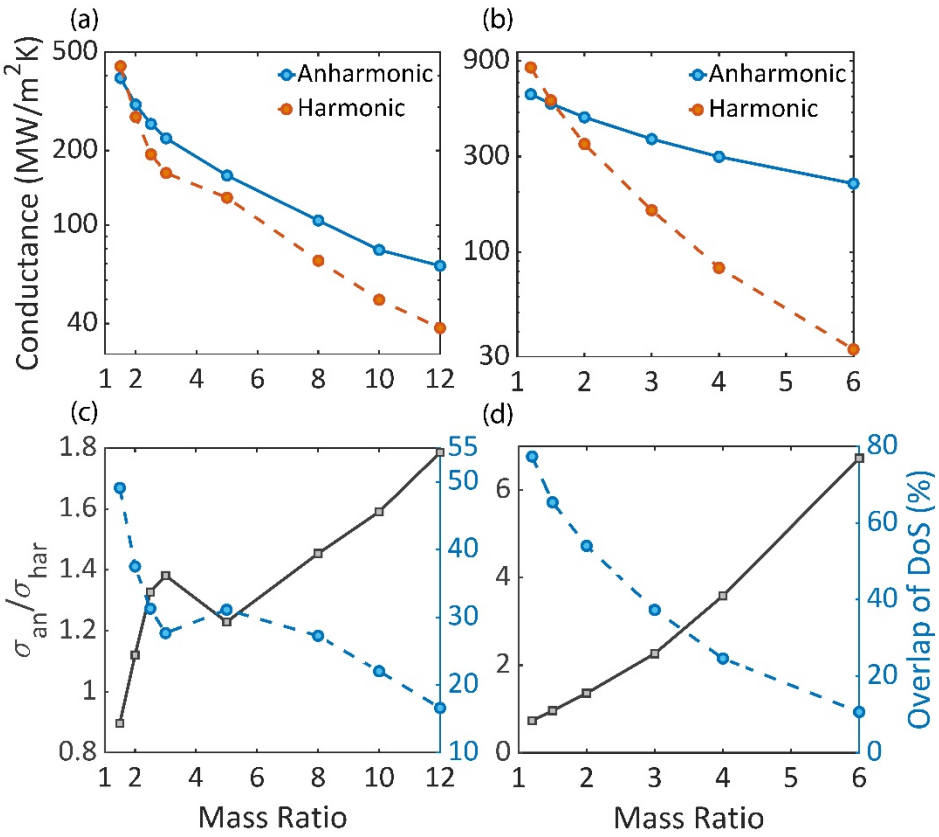

FIG. 2 (a)&(b) Conductance value as a function of mass ratio at 300K, for Si (a) and Al (b). The structure models used for anharmonic AGF are illustrated in the insets; (c)&(d) Thermal conductance ratio and overlap of versus mass ratio, for Si (c) and Al (d).

In order to explore the generality of the conductance enhancement for different interfaces, we performed further calculations on Si- and aluminum (Al)-based interfaces. We kept the left side to be Si or Al and varied the atomic mass on the right side by multiplying a mass ratio. As mass ratio increases, the absolute values of interfacial thermal conductance reduce in both harmonic and anharmonic cases, as shown in Fig. 2(a) and 2(b). When the mass ratio is close to one, the interface behaves more like the pure material so that the included three-phonon scattering acts as a barrier for phonon transport and inhibits the otherwise perfect transmission. For the Si-based interface, as illustrated in Fig. 2(c), the conductance ratio increases to a local maximum and then slightly decreases before the conductance ratio keeps increasing. In contrast, the conductance ratio of the Al-based interface monotonically increases, as plotted in Fig.2(d). In other words, the effects of anharmonicity are strongly system-dependent.

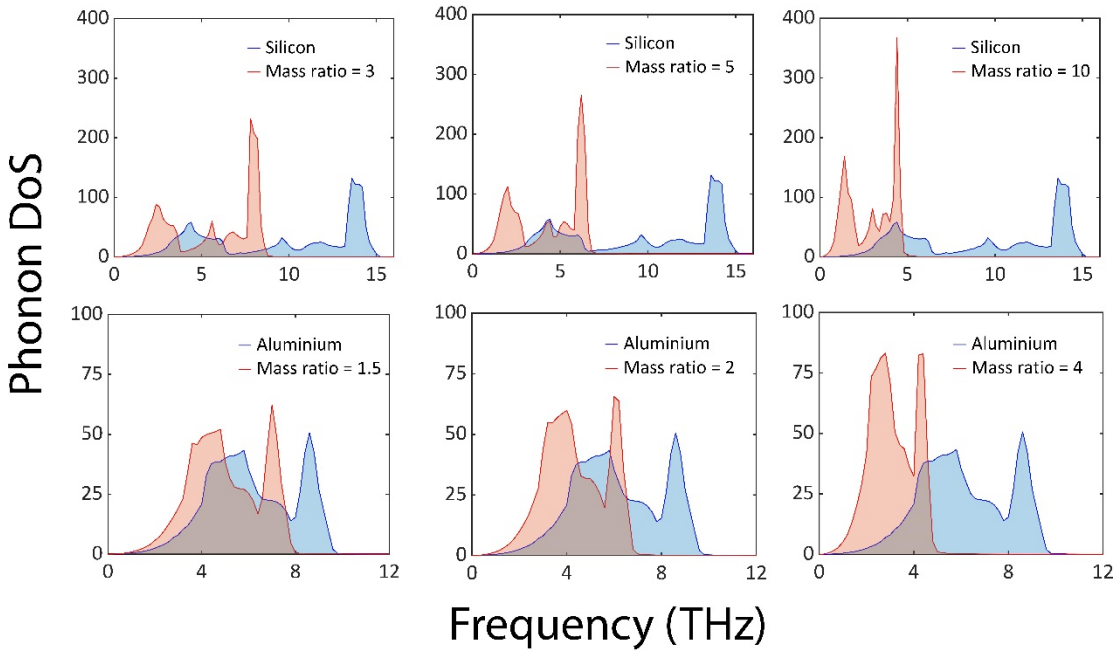

FIG. 3 DoS of the Si- or Al-based interface with different mass ratios; the blue one is Si or Al, while the red one is the DoS on the other side assigned with a different mass.

To understand the different conductance behaviors between Si and Al, the phonon DoS on both sides is shown in Fig. 3. The DoS mismatch will suppress allowed phonon channels in the harmonic case. The more disallowed channels in the harmonic regime, the more transmission channels anharmonicity can potentially enable. To illuminate the interplay of prohibited phonon channels and anharmonic effect, we used the overlap of DoS to represent the available phonon channels in the harmonic case. As shown in Fig. 3, different materials have different DoS, and this leads to different trends in the overlap area as the mass ratio increases. The thermal conductance ratio vs. mass ratio changes in exactly the opposite trend as the overlap of DoS vs. mass ratio for both Si and Al cases, as shown in Fig. 2 (c) & (d). In other words, if there are more channels for anharmonicity to open, the ratio of anharmonic vs. harmonic conductance is larger. As for the local maximum conductance ratio in the Si case is fundamentally due to the shape of DoS of silicon, which is an intrinsic material property. In brief, we quantitatively revealed the intrinsic mechanism for the enhanced thermal conductance by anharmonicity, for the first time.

Conclusion

In summary, we established a rigorous formalism of anharmonic AGF to include the anharmonicity at interfaces for the 3-D structures using first-principles force constants. More specifically, we developed a new Fourier decomposition method for 3rd order tensors and introduced the three-phonon scattering at solid-solid interfaces via the many-body self-energy in the reciprocal space without approximation. We observed an increase in thermal conductance at the Si/Ge interface due to anharmonicity in the central region. The new 3-D anharmonic AGF formalism enabled new understanding of phonon transport at interfaces -- the smaller DoS overlap at both the Si-based and Al-based interfaces, the more significant role anharmonicity

plays. Except for the case study performed in this work, we will investigate the further application of this method to different sizes and types of devices in the future. By overcoming the long-standing challenges of including anharmonicity into AGF for 3-D structures, we remarkably extended the application scope of AGF.

Acknowledgment

We thank Renjiu Hu for his help on 1-D anharmonic AGF calculation. We thank Chen Li for helping us with the force constants calculations. This work is sponsored by the Department of the Navy, Office of Naval Research under ONR award number N00014-18-1-2724. This work used the Extreme Science and Engineering Discovery Environment (XSEDE), which is supported by National Science Foundation grant number ACI-1053575.

Reference

[1] D. G. Cahill, P. V. Braun, G. Chen, D. R. Clarke, S. Fan, K. E. Goodson, P. Keblinski, W. P. King, G. D. Mahan, A. Majumdar, H. J. Maris, S. R. Phillpot, E. Pop, and L. Shi, Appl. Phys. Rev. **1**, 011305 (2014).

[2] D. Li and A. J. H. McGaughey, Nanoscale Microscale Thermophys. Eng. **19**, 166 (2015).

[3] N. Mingo and L. Yang, Phys. Rev. B **68**, 245406 (2003).

[4] S. Sadasivam, Y. Che, Z. Huang, L. Chen, S. Kumar, and T. S. Fisher, Annu. Rev. Heat Transf. **17**, pp. 89 (2014).

[5] W. Zhang, T. S. Fisher, and N. Mingo, J. Heat Transfer **129**, 483 (2007).

[6] D. A. Stewart, I. Savic, and N. Mingo, Nano Lett. **9**, 81 (2009).

[7] Z. Tian, K. Esfarjani, and G. Chen, Phys. Rev. B **86**, 235304 (2012).

[8] Z.-Y. Ong and G. Zhang, Phys. Rev. B **91**, 174302 (2015).

[9] S. Sadasivam, U. V. Waghmare, and T. S. Fisher, Phys. Rev. B **96**, 174302 (2017).

[10] Z. Y. Ong, Phys. Rev. B **98**, 195301 (2018).

[11] X. Li and R. Yang, Phys. Rev. B **86**, 054305 (2012).

[12] X. Li and R. Yang, J. Phys. Condens. Matter **24**, 155302 (2012).

[13] H. K. Lyeo and D. G. Cahill, Phys. Rev. B **73**, 144301 (2006).

[14] J. T. Gaskins, G. Kotsonis, A. Giri, S. Ju, A. Rohskopf, Y. Wang, T. Bai, E. Sachet, C. T. Shelton, Z. Liu, Z. Cheng, B. M. Foley, S. Graham, T. Luo, A. Henry, M. S. Goorsky, J. Shiomi, J. P. Maria, and P. E. Hopkins, Nano Lett. **18**, 7469 (2018).

[15] N. Mingo, Phys. Rev. B **74**, 125402 (2006).

[16] M. Luisier, Phys. Rev. B **86**, 245407 (2012).

[17] K. Miao, S. Sadasivam, J. Charles, G. Klimeck, T. S. Fisher, and T. Kubis, Appl. Phys. Lett. **108**, 113107 (2016).

[18] S. Sadasivam, N. Ye, J. P. Feser, J. Charles, K. Miao, T. Kubis, and T. S. Fisher, Phys. Rev. B **95**, 085310 (2017).

[19] LV Keldysh, Sov. Phys. JETP **20**, 1018 (1965).

[20] S. Datta, *Electronic Transport in Mesoscopic Systems* (Cambridge university press, 1997).

[21] A. P. Jauho, N. S. Wingreen, and Y. Meir, Phys. Rev. B **50**, 5528 (1994).

[22] H. Haug and A.-P. Jauho, *Quantum Kinetics in Transport and Opttics of Semiconductors* (Berlin: Springer, 2008).

[23] T. Feng, Y. Zhong, J. Shi, and X. Ruan, Phys. Rev. B **99**, 045301 (2019).

[24] See Supplemental Material at [URL] for details about this section.

[25] N. Mingo, *Green's Function Methods for Phonon Transport Through Nano-Contacts* (Springer, Berlin, Heidelberg, 2009).

[26] J. S. Wang, J. Wang, and J. T. Lü, Eur. Phys. J. B **62**, 381 (2008).

[27] F. Guinea, C. Tejedor, F. Flores, and E. Louis, Phys. Rev. B **28**, 4397 (1983).

[28] L. De Lathauwer, 2009 IEEE Int. Symp. Circuits Syst. 2773 (2009).

[29] M. E. Kilmer and C. D. Martin, Linear Algebra Appl. **435**, 641 (2011).

[30] E. M. Lifshitz and L. P. Pitaevskii, *Course of Theoretical Physics: Physical Kinetics* (Pergamon, Oxford, 1981).

[31] P. Giannozzi, O. Andreussi, T. Brumme, O. Bunau, M. Buongiorno Nardelli, M. Calandra, R. Car, C. Cavazzoni, D. Ceresoli, M. Cococcioni, N. Colonna, I. Carnimeo, A. Dal Corso, S. De Gironcoli, P. Delugas, R. A. Distasio, A. Ferretti, A. Floris, G. Fratesi, G. Fugallo, R. Gebauer, U. Gerstmann, F. Giustino, T. Gorni, J. Jia, M. Kawamura, H. Y. Ko, A. Kokalj, E. Kücükbenli, M. Lazzeri, M. Marsili, N. Marzari, F. Mauri, N. L. Nguyen, H. V. Nguyen, A. Otero-De-La-Roza, L. Paulatto, S. Poncé, D. Rocca, R. Sabatini, B. Santra, M. Schlipf, A. P. Seitsonen, A. Smogunov, I. Timrov, T. Thonhauser, P. Umari, N. Vast, X. Wu, and S. Baroni, J. Phys. Condens. Matter **29**, 465901 (2017).

[32] P. Giannozzi, S. Baroni, N. Bonini, M. Calandra, R. Car, C. Cavazzoni, D. Ceresoli, G. L. Chiarotti, M. Cococcioni, I. Dabo, A. Dal Corso, S. De Gironcoli, S. Fabris, G. Fratesi, R. Gebauer, U. Gerstmann, C. Gougoussis, A. Kokalj, M. Lazzeri, L. Martin-Samos, N. Marzari, F. Mauri, R. Mazzarello, S. Paolini, A. Pasquarello, L. Paulatto, C. Sbraccia, S. Scandolo, G. Sclauzero, A. P. Seitsonen, A. Smogunov, P. Umari, and R. M. Wentzcovitch, J. Phys. Condens. Matter **21**, 395502 (2009).

[33] A. Togo and I. Tanaka, Scr. Mater. **108**, 1 (2015).

[34] W. Li, J. Carrete, N. A. Katcho, and N. Mingo, Comput. Phys. Commun. **185**, 1747 (2014).